RSC Advances

PAPER

View Article Online
View Journal | View Issue

Cite this: *RSC Adv.*, 2023, **13**, 10254

The polar and nonpolar interfaces influenced of magnetism in $LaMnO_3$-based superlattices

Guowei Zhou, *[ab] Zhilan Li,[a] Jiarui Dou,[a] Huihui Ji,[ab] Penghua Kang,[a] Yufan Shen,[a] Siqi Wang[a] and Xiaohong Xu*[ab]

Received 12th January 2023
Accepted 28th March 2023

DOI: 10.1039/d3ra00229b

rsc.li/rsc-advances

The interface of perovskite heterostructures has been shown to exhibit various electronic and magnetic phases such as two-dimensional electron gas, magnetism, superconductivity, and electronic phase separation. These rich phases are expected due to the strong interplay between spin, charge, and orbital degree of freedom at the interface. In this work, the polar and nonpolar interfaces are designed in $LaMnO_3$-based (LMO) superlattices to investigate the difference in magnetic and transport properties. For the polar interface in a LMO/$SrMnO_3$ superlattice, a novel robust ferromagnetism, exchange bias effect, vertical magnetization shift, and metallic behaviors coexist due to the polar catastrophe, which results in a double exchange coupling effect in the interface. For the nonpolar interface in a LMO/$LaNiO_3$ superlattice, only the ferromagnetism and exchange bias effect characteristics exist due to the polar continuous interface. This is attributed to the charge transfer between Mn^{3+} and Ni^{3+} ions at the interface. Therefore, transition metal oxides exhibit various novel physical properties due to the strong correlation of d electrons and the polar and nonpolar interfaces. Our observations may provide an approach to further tune the properties using the selected polar and nonpolar oxide interfaces.

Introduction

The transition metal oxide heterostructures offer better physical properties than the corresponding bulk materials. Some unexpected and remarkable characteristics have been discovered at interfaces of these oxide heterostructures. Such characteristics provide potential technological and fundamental conditions for future perovskite oxide-based devices.[1–5] In the meantime, the atomic-level precise control of thin film growth is possible, providing the opportunity to couple different physical properties at the microscopic level. The underlying goal is to find unusual interfacial phenomena compared to conventional thin films.[6,7] Recently, the $LaAlO_3$/$SrTiO_3$ (LAO/STO) heterostructure has received much attention because of its unique polar interface. This unique polar interface possesses a lot of novel phenomena, such as interfacial magnetism, superconductivity, and metallic gas or insulating behavior under varying circumstances.[8–13]

This study explores the coupling of different polar materials with manganese oxides and compares the properties of their interfaces. A type A antiferromagnetic (AFM) insulator, $LaMnO_3$ (LMO), is coupled with the paramagnetic (PM) metal $LaNiO_3$ (LNO) and G-type antiferromagnetic insulator $SrMnO_3$ (SMO). For the LMO/SMO superlattice, we show that the polar catastrophe, arising from the alternately charged LMO layers and neutral SMO layers, is quenched by accumulating an extra half electron per cell in the interface region, similar to the case of the LAO/STO interface.[14] The two-dimensional conductivity at the LAO/STO interface was initially explained in terms of the so-called polar-catastrophe scenario.[15,16] Conversely, the LMO and LNO materials are both alternately charged, hence, they are polar continuous. The LMO/SMO superlattices show different transport properties and magnetism compared with the polar continuous LMO/LNO superlattice. As is known to all, polar discontinuity is an important driving force for regulating the oxide heterostructure interfaces. Moreover, many studies show that for the heterostructures with polar discontinuity will significantly impact the physical properties, such as the magnetic property and electrical transport of the heterostructure. That is why polar interfaces have attracted much attention. Our work further specifically compares the properties exhibited by coupling to different heterogeneous structures, which provides a basis for improving the performance of oxide devices.

Experimental

High quality epitaxial $[LMO(3)/SMO(2)]_{10}$ and $[LMO(3)/LNO(2)]_{10}$ superlattices were deposited on $SrTiO_3$ (001) substrates by pulsed laser deposition system (PLD). For

[a]School of Chemistry and Materials Science of Shanxi Normal University, Key Laboratory of Magnetic Molecules and Magnetic Information Materials of Ministry of Education, Taiyuan 030006, China. E-mail: zhougw@sxnu.edu.cn

[b]Research Institute of Materials Science of Shanxi Normal University, Collaborative Innovation Center for Shanxi Advanced Permanent Magnetic Materials and Techonology, Taiyuan 030006, China. E-mail: xuxh@sxnu.edu.cn

convenience, these two superlattices were labeled as L3S2 and L3L2, respectively. For comparison, the LMO, SMO, and LNO single thin films as 30 unit cells (u.c.) were grown as well. All these samples were monitored using the *in situ* reflection high energy electron diffraction (RHEED) during deposition process. These superlattices were grown at a temperature of 725 °C and the oxygen pressure at 100 mTorr. After that, the samples were *in situ* annealed for one hour under an oxygen pressure of 300 Torr. The crystal structures were characterized by high-resolution four circle X-ray diffraction meter. The in-plane magnetic hysteresis loops were measured with physical properties measurement system (PPMS) and superconducting quantum interference device (SQUID). The magnetic hysteresis loops were received after subtracting the diamagnetic background of plastic tube and STO substrate. The electrical transport measurements were performed using a linear four-probe configuration with the magnetic field perpendicular to the current direction. The X-ray absorption spectroscopy (XAS) curves of Mn and Ni L-edge in these samples were measured at the beamline BL12B-a and the BL08U1A of the of the National Synchrotron Radiation Laboratory (NSRL) and Shanghai Synchrotron Radiation Facility (SSRF), respectively. The absorption signal were detected by the total electron yield (TEY) method and the background vacuum level was kept as 6×10^{-6} Torr. The XAS spectra were normalized to result in the pre-edge spectral region of L_3 as zero and the peak at the L_3 edge as one.

Results and discussion

XRD measurements were conducted to measure the crystalline quality of the samples. Fig. 1a displays representative XRD spectra measured around (002) peak for five samples. Clear superlattices of Bragg peaks and the SL ± 1 satellite peaks are observed in these spectra. It indicates a high-quality deposition of the samples.[17] To further demonstrate the growth of the superlattice was monitored *in situ* using the RHEED system. Fig. 1b and c show diffraction patterns of the STO substrate before starting the growth process (left) and the superlattice at the end of the growth process (right), together with partial RHEED oscillating curves.[18] The apparent large-amplitude oscillation and the bright diffraction spots indicate that the films grow layer-by-layer during the deposition process. It is sufficient to prove a high epitaxial quality and smooth surface. The data in Fig. 1 provides favorable conditions to explore the magnetic and transport properties of the superlattice.

Many studies have found that transition-metal-oxide heterostructure interfaces show excellent properties.[19–22] The symmetry damage at the interface, electrostatic coupling, polar disaster, and atomic rearrangement of the heterostructures all significantly influence the interface. Among them, polar interfaces have been of particular interest to researchers because extra electrons may migrate to the interface to heal the polar catastrophe. Under varying circumstances, these interfacial electrons may exhibit unusual properties, such as the Kondo resistance minimum, superconductivity, magnetism, and metallic or insulating behavior. Specifically, when polar materials are deposited on an electro-neutral substrate, a polar disaster occurs at the interface. For the perovskite structure of LMO/SMO, LMO consists of alternating positively charged LaO^{+1} and negatively charged MnO^{-1} layers along the (001) direction. Moreover, SMO is configurated with neutral SrO^{0} and MnO20 layers. In the LMO/SMO interface context, alternately

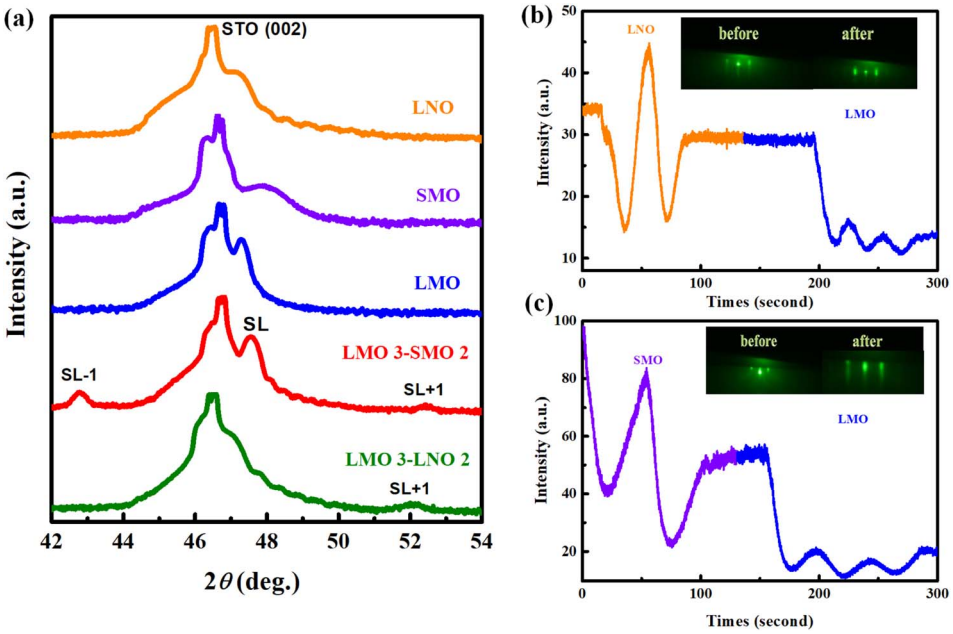

Fig. 1 (a) X-ray diffraction θ–2θ scan around the (002) peak for LNO, SMO, LMO single films and L3S2, L3N2 superlattices. The first-order superlattice reflections are denoted as SL ± 1. A partial oscillation curves of the specular beam during the growth of (b) LMO (3 u.c.)/SMO (2 u.c.) and (c) LMO (3 u.c.)/LNO (2 u.c.) superlattices. The insets are the *in situ* RHEED images before and after the growth processes.

stacked positive and negative layers of LaO and MnO_2 lead to a divergent Coulomb potential, also called a polar catastrophe. However, polar catastrophe induces a considerable energy loss for atomically abrupt heterointerfaces between planes of different polarity. It is the interface analog of the divergent surface energy that would result from terminating a material along a polar plane with no surface reconstruction. In this work, the positive charge in the LaO plane spontaneously donates about half an electron to the neighboring MnO_2 plane. It is quenched by accumulating an extra half electron per cell in the interface region, similar to LAO/STO interface polar catastrophe.[23–25] The interface analog of the divergent surface energy is shown in Fig. 2a. It shows how an atomically abrupt interface between polar and neutral layers leads to a polar catastrophe where the electrostatic potential diverges with thickness.

Moreover, there is a fundamental asymmetry in charge density. In the context of the LMO/SMO interface, if there is no redistribution of charges at the interface, it will lead to a tremendous electrostatic potential inside the heterostructure, because of which the stability is reduced. Therefore, the charges inside the system will rearrange to reduce this impact, eventually leading to drastic changes in the interface properties of the heterostructure. Unlike conventional semiconductors where each ion has a fixed valence, mixed valence charge compensation occurs in complex oxides if electrons can be redistributed at lower energy loss than ions. Conceptually, one can first construct the interface from neutral atoms and then allow ionization, resulting in the net transfer of half an electron per two-dimensional unit cell (e^- per u.c.) from LaO to MnO_2 across the interface (Fig. 2b). This process leaves the overall structure neutral, with the Mn ion at the interface becoming $Mn^{3.5+}$, and also the potential no longer diverges. We have plotted the initial potential of the charged layers and the final potential after charge reconstruction. On the contrary, the LMO layer contains LaO^{+1} and $MnO_2{}^{-1}$ planes, and the LNO layer consists of LaO^{+1} and $NiO_2{}^{-1}$ planes, as shown in the Fig. 2c. As a result, there is no polar disaster or a fundamental symmetry in charge density and the potential is no longer divergent as well.

The polarization catastrophe in the perovskite heterostructures plays a vital role. It can induce unexpected interfacial magnetic and electronic properties. Specifically, the polar mismatch induced charge-redistribution can lead to strong ferromagnetism. As shown in Fig. 3a, the fixed thicknesses of LMO and SMO layers are 3 u.c. and 2 u.c., respectively, for each period in the L3S2 superlattice, and the same goes for LMO 3–LNO 2 (L3L2) superlattice. Each superlattice grew in 10 cycles. Among the SMO, LMO and LNO, the hysteresis loop of LNO and SMO layers is a straight line across the center, indicating that under this experimental condition, the obtained LNO and SMO films do not show magnetism, which is consistent with their bulk properties. The LMO bulk material exhibits AFM characteristic of the ground state, where Mn magnetic moments are arranged in an A-type AFM ordering.[26] The state of this structure is in in-plane spin alignment, which is in the same direction, showing a ferromagnetic ordering. However, the out-of-plane spin alignment is the opposite, showing an antiferromagnetic ordering. Compared with other antiferromagnetic structures, this LMO thin film is easily affected by oxygen pressure and defects during sample preparation. Such a type of LMO thin film produces ferromagnetism through spin tilt. Notably, the ferromagnetic insulating behavior is present in LMO thin films. Hence, a hysteretic character can be observed in the figures.[27–30] The saturated magnetization of the L3S2 superlattice is larger than the L3L2 superlattice. Fig. 3b and c display the in-plane and out-of-plane magnetic hysteresis loops measured at 5 K for these two LMO-based heterostructures. It is obvious that the saturated magnetization is larger along the in-plane direction than that along the out-of-plane direction for L3S2 superlattices. Hence, the easy magnetization axis is along the in-plane direction. Similarly, Fig. 3c shows the magnetic hysteresis loops of the L3L2 superlattices. It's consistent with L3S2 superlattice that the easy magnetization axis is along the in-plane direction.

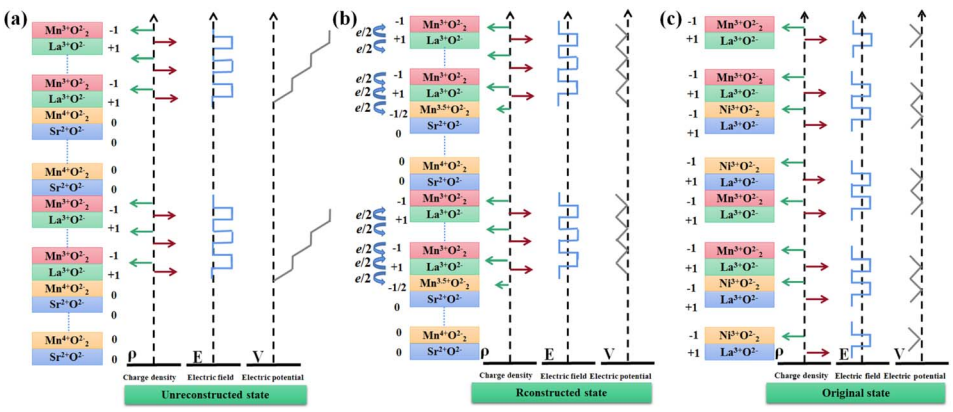

Fig. 2 (a) The alternating charges of the LMO and the neutral charges of the SMO generate a positive average electric field (E), charge density (ρ) and a diverging potential (V). (b) Schematic diagram of discontinued polarization at the interfaces of LMO/SMO superlattices. The system electronically reconstructs LMO film by transferring half an electron per unit cell from the surface to the interface. (c) The schematic diagram at the interfaces of LMO/LNO superlattices.

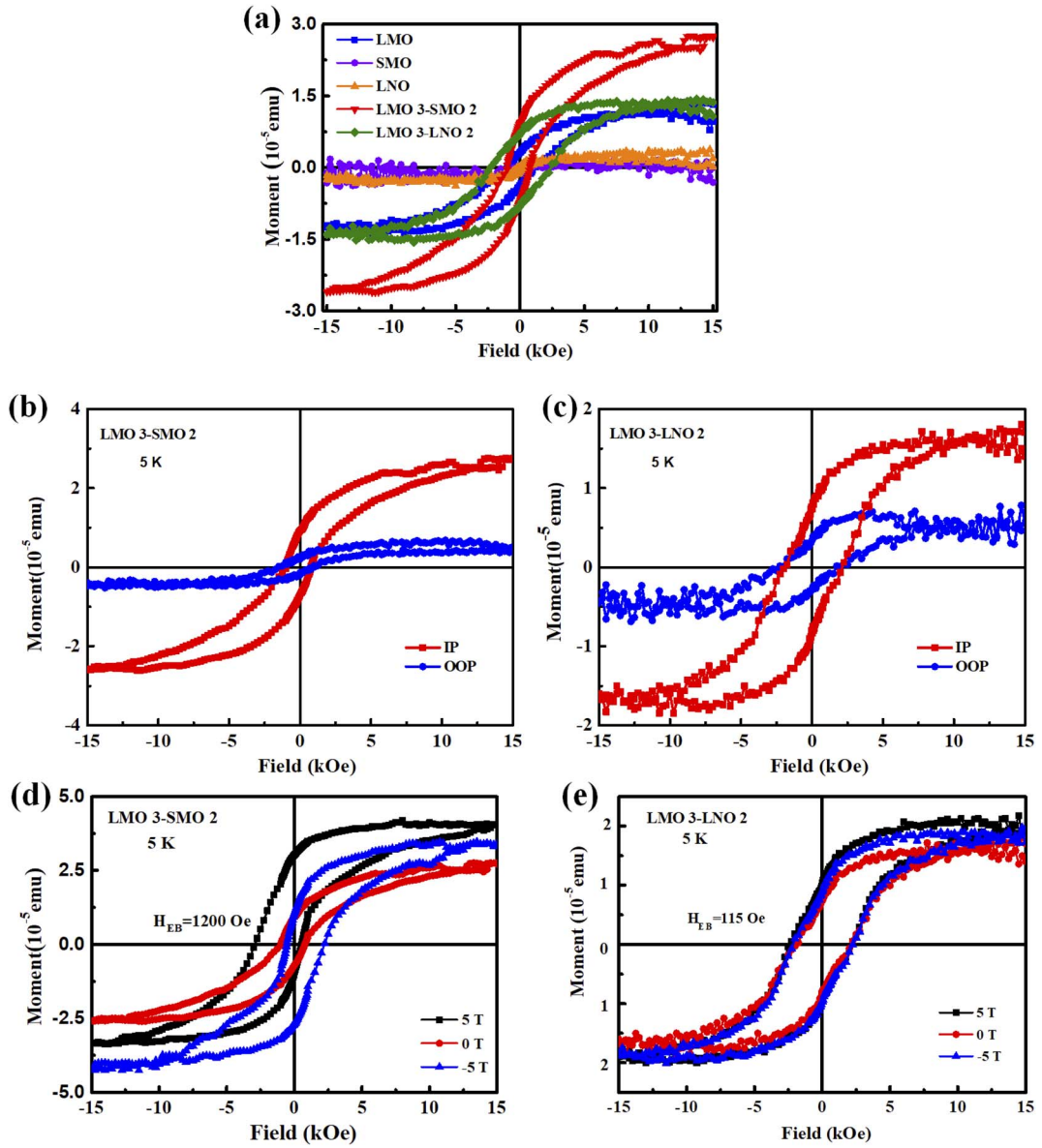

Fig. 3 (a) Hysteresis loops of the LMO, SMO, LNO, L3S2, and L3L2 samples were measured at 5 K after zero-field cooling from room temperature. The magnetic hysteresis loops along in-plane (IP) and out-of-plane (OOP) directions for (b) LMO(3)–SMO(2) and (c) LMO(3)–LNO(2) superlattices. Magnetic hysteresis loops measured at 5 K after cooling from room temperature under different in-plane fields (±5 T) and zero-field cooling process for (d) LMO(3)–SMO(2) and (e) LMO(3)–LNO(2) superlattices.

Fig. 3d and e present the measured magnetic hysteresis loops after field-cooling from room temperature to 5 K in a ±5 T field. As shown in Fig. 3d, L3S2 presents a ferromagnetic behavior, and the direction of the horizontal loop shift is opposite to that of the cooling field for all the samples. In general, a shift of loop along the magnetic field axis is quantified using the equations such as exchange field (H_{EB}) and coercivity (H_C): $H_{EB} = |H_+ + H_-|/2$ and $H_C = |H_+ - H_-|/2$, where H_+ and H_- denote the right and left values of the coercivity, respectively. After field cooling from room temperature to 5 K in the presence of a +5 T field, the H_+ and H_- are 518 and −2918 Oe. It indicates the EB field and the coercivity values of 1200 and 1718 Oe. Meanwhile, the 840 Oe shift of the magnetic loop under the −5 T field along the magnetic field axis is observed towards the positive field, and the value of the coercive field is 1390 Oe. This phenomenon suggests the exchange bias effect in the L3S2 superlattices. Among other things, the vertical magnetization shift (VMS) refers to the offset of the hysteresis loop along the magnetization axis. In the L3S2 superlattices, the saturation magnetization (M_S) is much more prominent on the positive-field side than on the negative-field side when the sample is cooled in a positive field. Then, when the sample is cooled in the negative field, the M_S of the negative field side is much larger than that of the positive field side. So, the direction of the cooling field is the critical factor that determines the directions of the horizontal shift along the field axis and the

vertical shift along the magnetization axis. Accordingly, the VMS phenomenon is obvious in the L3S2 superlattices. The coexistence of strong EBE and VMS is observed in the L3S2 superlattices. Based on the previous reports, the FM states are expected to be induced at the interfaces for all L3S2 superlattices.[31–33] The thickness dependence of the orbital reconstruction induces the canted AFM states in the LMO layer. Consequently, the FM states at the interface compete with the canted AFM states in the LMO layers, resulting in the coexistence of the exchange bias effect and VMS phenomena in the L3S2 superlattices.

Meanwhile, in another experiment the transfer of charges is found to be responsible for the variable magnetic properties. As shown in Fig. 3e, for the L3L2 superlattices, the 115 Oe shift of the magnetic loop along the magnetic field axis is observed towards negative field values after field cooling from room temperature to 5 K in the presence of a +5 T field whose value is calculated as $H_C = 2275$ Oe. It suggests the presence of the exchange bias effect in L3L2. On the contrary, the 52 Oe shift of the magnetic loop along the magnetic field axis under a −5 T field is observed towards positive field values with $H_C = 2202$ Oe.[34] This effect is attributed to the interfacial charge transfer from Mn to Ni ions that induces localized magnetic moments to pin the ferromagnetic LMO layer. The L3L2 superlattice has a weaker EBE, a smaller saturation magnetization, and a lower Curie temperature than L3L2. It is the difference in polarity that leads to the different phenomena.

In addition, to gain insight into transport properties in samples, we focus on the prototypical perovskite heterointerface. Fig. 4a presents the temperature dependence of resistance curves for samples. The transport characteristics of LMO and SMO grew on strontium titanate substrate under identical conditions were insulating. However, LNO exhibits metallic behavior. As previously reported, the SMO material is a band insulator while the LMO material is a Mott insulator. As for LNO, the transport property of the material changes from a metal state to an insulating state with a change in thickness.[35–37] Our experiment is consistent with the literature. Moreover, the L3S2 superlattices undergo the insulator–metal–insulator transition as the temperature increases. This transition can be associated with the complex magnetic structure in the superlattices.[18] Direct current transport measurements for the L3L2 are shown in Fig. 4a, where the insulating behavior is still present. This feature is attributed to the insulating character of thinner LNO-based superlattices, induced by the reduced dimensionality. Fig. 4b shows the temperature dependence of the magnetic moments for a series of samples over a temperature range of 5–310 K. It corresponds to the properties exhibited by Fig. 3a. The saturation magnetization of the L3S2 superlattice is larger than that of the L3L2 superlattice. LMO possesses weak magnetism, while LNO and SMO do not show any magnetism. So, the interface ferromagnetism present in the superlattice of the sample can be supported by the macroscopic magnetism and transport measurements.

Next, we elaborate on the origin of interfacial ferromagnetism in the L3S2 and L3L2 superlattices. There are mainly two explanations for the ferromagnetism of the interface in non-magnetic oxide heterostructures. The one is that the traveling electrons in the metal layer at the heterostructure interface are transferred to the adjacent insulating layer, which leads to the ferromagnetic double exchange. The other is that the generation of ferromagnetism at the interface is related to the polar discontinuity in the system. The existence of polar discontinuity leads to an electrostatic potential at the interface of the heterostructure, which aggravates the instability of the system. In order to eliminate the electrostatic potential, charge reconfiguration occurs at the interface of the heterostructure, and then the interface ferromagnetism is induced.

To explore the origin of this disparity in the magnetic behavior and transport properties in superlattices, we performed X-ray absorption spectroscopy (XAS) measurements. In other words, XAS is used to characterize the transfer of charge on the interface, including changes in the valence states of Ni and Mn ions in the superlattices. It is mainly measured near the Mn $L_{3,2}$ absorption edge, and uses elements to detect the microelectronic properties near the interface. Fig. 5a displays

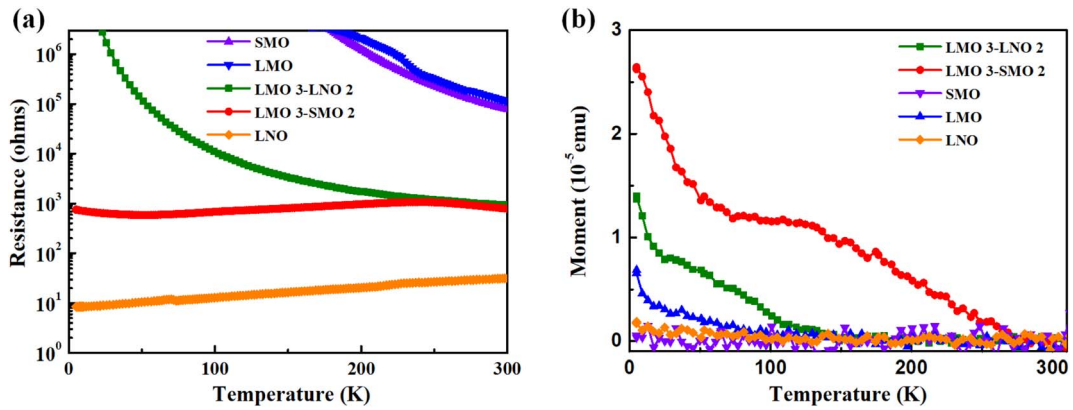

Fig. 4 (a) Temperature dependence of the resistance of L3L2, and L3S2 superlattices and the SMO, LMO, and LNO films as reference samples. (b) Magnetic moments of the L3L2, and L3S2 superlattices and the SMO, LMO, and LNO films were measured as a function of temperature with an in-plane magnetic field of 500 Oe.

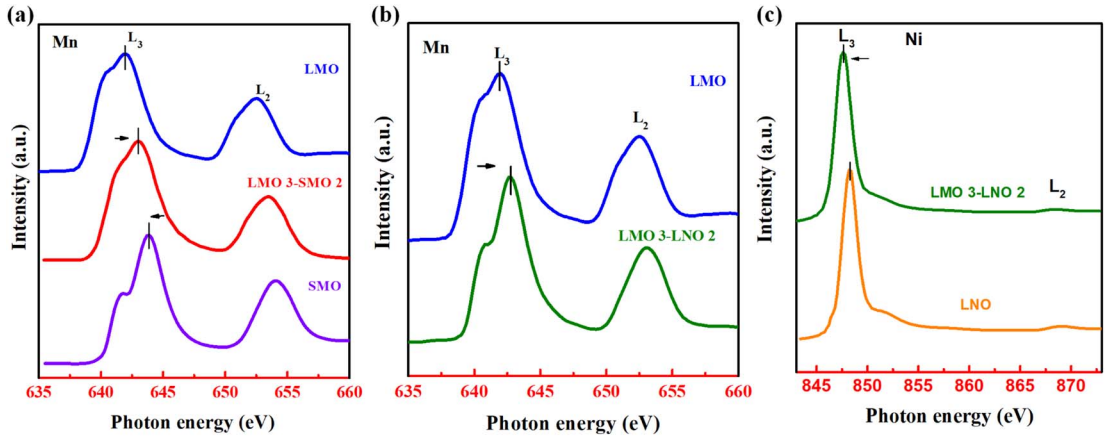

Fig. 5 (a–c) Normalized XAS spectra at the Mn L-edge and Ni L-edge for different samples at room temperature. Arrows mark the variation around the Mn L-edge and Ni L-edge.

the XAS spectra of the L3S2 superlattice. Compared with a single LMO and SMO film, the Mn L_3 edge of L3S2 significantly shifts. The energy splitting between the L_2 and L_3 edges is about 10.0 eV and the area ratio of L3S2 peaks is roughly 2 : 1. These results suggest the valency of Mn ions of L3S2 to be in the range of +3.8 to +4.0.[38] Therefore, it can be inferred from the valence state change those polar discontinuities in the L3S2 superlattice drives the interfacial charge redistribution. This interfacial charge redistribution involves the leakage of itinerant electrons giving rise to the double exchange, which causes the emergence of ferromagnetism.[39–42] As mentioned above, the superlattice sample at the interface shows in-plane ferromagnetism due to double exchange. However, the LMO layer shows a tilted AFM state. It leads to an exchange bias effect. Fig. 5b and c shows the XAS spectra of the L3L2 and the single LMO and LNO films near the L edge of Mn and Ni elements. As known, the Mn valence state in the monolayer LMO material is +3. The Mn L_3 edge peak is towards higher energy in the L3L2 superlattices. It points out that the Mn valence state changes from +3 to +4. In other words, the Mn at the interface loses an electron because of the charge transfer from interfacial Mn to Ni ions.[43] According to the Goodenough Kanamori rules, the coupling between Mn^{4+} and Ni^{2+} ions at this interface leads to super-exchange interaction. It proves that the interfacial exchange interaction between Mn and Ni contributes to magnetism. The exchange bias effect in the L3L2 is due to the pinning of ferromagnetic LMO by the localized magnetic moment at the interface.

Conclusions

Magnetic and charge transfer differences have been investigated in L3L2 and L3S2 superlattices. The L3S2 superlattice shows better transport properties and powerful magnetism than the L3L2 superlattice. It is considered that the double exchange effect prompts the interfacial ferromagnetic state in the L3S2 superlattice. At the same time, charge redistribution due to polar catastrophe also leads to ferromagnetism. The L3L2 superlattice has a charge transfer between Mn^{3+} and Ni^{3+} at the interface. This charge transfer process leads to ferromagnetic coupling between the cations. Therefore, transition metal oxides exhibit various novel physical properties due to the strong correlation of d electrons and the coupling between different degrees of freedom. Hence, polar materials are coupled to different materials and exhibit quite different properties. Polar discontinuities occurring at interfaces between two materials are both a challenge and an opportunity to study and develop devices.

Conflicts of interest

The authors have no conflicts to disclose.

Acknowledgements

This work is financially supported by the National Natural Science Foundation of China (No. 51901118, 51871137, 12174237, and 52171183), the 1331 Engineering of Shanxi Province, the Research Project Supported by Shanxi Scholarship Council of China (2021-093), and Shanxi Normal University Graduate Science and Technology Innovation Project (No. 2021XSY036). We acknowledge the XAS measurement at Beamline BL08U1A in Shanghai Synchrotron Radiation Facility (SSRF) and at Beamline BL12-a in National Synchrotron Radiation Laboratory (NSRL).

References

1 S. Okamoto and A. J. Millis, *Nature*, 2004, **428**, 630.
2 A. Ohtomo and H. Y. Hwang, *Nature*, 2004, **427**, 423.
3 A. Gozar, G. Logvenov, L. F. Kourkoutis, A. T. Bollinger, L. A. Giannuzzi, D. A. Muller and I. Bozovic, *Nature*, 2008, **455**, 782.
4 P. Zubko, S. Gariglio, M. Gabay, P. Ghosez and J. M. Triscone, *Annu. Rev. Condens. Matter Phys.*, 2011, **2**, 141.
5 H. Y. Hwang, Y. Iwasa, M. Kawasaki, B. Keimer, N. Nagaosa and Y. Tokura, *Nat. Mater.*, 2012, **11**, 103.

6 J. Chakhalian, J. W. Freeland, A. J. Millis, C. Panagopoulos and J. M. Rondinelli, *Rev. Mod. Phys.*, 2014, **86**, 1189.
7 J. H. Ngai, F. J. Walker and C. H. Ahn, *Annu. Rev. Mater. Res.*, 2014, **44**, 1.
8 K. Wang, M. H. Tang, Y. Xiong, G. Li, Y. G. Xiao, W. L. Zhang, Z. P. Wang, Z. Li and J. He, *RSC Adv.*, 2017, **7**, 31327.
9 A. Brinkman, M. Huijben, M. V. Zalk, J. Huijben, U. Zeitler, J. C. Maan, D. W. W. G. van, G. Rijnders, D. H. A. Blank and H. Hilgenkamp, *Nat. Mater.*, 2007, **6**, 493.
10 S. Thiel, G. Hammerl, A. Schmehl, C. W. Schneider and J. Mannhart, *Science*, 2006, **313**, 1942.
11 M. Huijben, G. Rijnders, D. H. A. Blank, S. Bals, S. V. Alert, J. Verbeeck and G. V. Tendeloo, *Nat. Mater.*, 2006, **5**, 2235.
12 C. Cen, S. Thiel, G. Hammerl, C. W. Schneider, K. E. Andersen, C. S. Hellberg, J. Mannhart and J. Levy, *Nat. Mater.*, 2008, **7**, 298.
13 Z. S. Popović, S. Satpathy and R. M. Martin, *Rev. Mod. Phys.*, 2008, **101**, 256801.
14 A. H. Reshak, M. S. A. Jafar and Y. A. Douri, *J. Appl. Phys.*, 2016, **119**, 245303.
15 N. Nakagawa, H. Y. Hwang and D. A. Muller, *Nat. Mater.*, 2006, **5**, 204.
16 B. Paudel, I. Vasiliev, M. Hammouri, D. Karpov, A. P. Chen, V. Lauter and E. Fohtung, *RSC Adv.*, 2019, **9**, 13033.
17 J. Son, J. M. L. Beau, S. J. Allen and D. Ouellette, *Appl. Phys. Lett.*, 2010, **97**, 202109.
18 G. W. Zhou, H. H. Ji, W. Lin, J. L. Zhang, Y. H. Bai, J. S. Chen and X. H. Xu, *Phys. Rev. B*, 2020, **101**, 024422.
19 K. S. Takahashi, M. Kawasaki and Y. Tokura, *Appl. Phys. Lett.*, 2001, **79**, 1324.
20 Y. Jin, X. L. Qian, B. Lu, S. X. Cao and J. C. Zhang, *RSC Adv.*, 2015, **5**, 2354.
21 M. Gibert, P. Zubko and R. Scherwitzl, *Nat. Mater.*, 2012, **11**, 195.
22 J. F. Ding, O. I. Lebedev, S. Turner, Y. F. Tian, W. J. Hu, J. W. Seo, C. Panagopoulos, W. Prellier, G. Van Tendeloo and T. Wu, *Phys. Rev. B: Condens. Matter Mater. Phys.*, 2013, **87**, 054428.
23 N. Nakagawa, D. Muller, A. Ohtomo, L. G. John and H. Y. Hwang, *Nat. Mater.*, 2006, **5**, 657.
24 H. H. Ji, Z. Yan, W. G. Zhou, X. J. Wang, J. Zhang, Z. Q. Li, P. H. Kang and X. H. Xu, *Appl. Phys. Lett.*, 2020, **117**, 192402.
25 B. R. K. Nanda and S. Satpathy, *Phys. Rev. B: Condens. Matter Mater. Phys.*, 2010, **81**, 224408.
26 W. S. Choi, D. W. Jeong, S. Y. Jang, Z. Marton, S. S. A. Seo, H. N. Lee and Y. S. Lee, *J. Korean Phys. Soc.*, 2011, **58**, 569.
27 C. Ritter, M. R. Ibarra, J. M. D. Teresa, P. A. Algarabel, C. Marquina, J. Blasco, J. García, S. Oseroff and S. W. Cheong, *Phys. Rev. B: Condens. Matter Mater. Phys.*, 1997, **56**, 8902.
28 Y. S. Hou, H. J. Xiang and X. G. Gong, *Phys. Rev. B: Condens. Matter Mater. Phys.*, 2014, **89**, 064415.
29 G. W. Zhou, Z. Yan, Y. H. Bai, J. L. Zang, Z. Y. Quan, S. F. Qi and X. H. Xu, *ACS Appl. Mater. Interfaces*, 2017, **9**, 39855.
30 J. J. Peng, C. Song, B. Cui, F. Li, H. J. Mao, Y. Y. Wang, G. Y. Wang and F. Pan, *Phys. Rev. B: Condens. Matter Mater. Phys.*, 2014, **89**, 165129.
31 Y. R. Wang, Z. B. Yang, F. L. Lu, C. Jin, J. Wu, M. Shen, R. Z. Yang and F. L. Chen, *RSC Adv.*, 2015, **5**, 974.
32 H. B. Zhao, K. J. Smith, Y. Fan, G. Lupke, A. Bhattacharya, S. D. Bader, M. Warusawithana, X. Zhai and J. N. Eckstein, *Phys. Rev. Lett.*, 2008, **100**, 117208.
33 A. Bhattacharya, S. J. May, S. G. E. T. Velthuis, M. Warusawithana, X. Zhai, B. Jiang, J. M. Zuo, M. R. Fitzsimmons, S. D. Bader and J. N. Eckstein, *Phys. Rev. Lett.*, 2008, **100**, 257203.
34 M. Gibert, M. Viret, P. Zubko, N. Jaouen, J. M. Tonnerre, A. TorresPardo, S. Catalano, A. Gloter, O. Stéphan and J. M. Triscone, *Nat. Commun.*, 2016, **7**, 1.
35 A. Galdi, C. Aruta, P. Orgiani, C. Adamo, V. Bisogni, N. B. Brookes, G. Ghiringhelli, D. G. Schlom, P. Thakur and L. Maritato, *Phys. Rev. B: Condens. Matter Mater. Phys.*, 2012, **85**, 124129.
36 I. Marozau, P. T. Das, M. Dbeli, J. G. Storey and C. Bernhard, *Phys. Rev. B: Condens. Matter Mater. Phys.*, 2014, **89**, 174422.
37 S. J. May, T. S. Santos and A. Bhattacharya, *Phys. Rev. B: Condens. Matter Mater. Phys.*, 2009, **79**, 115127.
38 M. G. Proietti, G. Subias, J. Garca, M. C. Snchez and J. Blasco, *Surf. Rev. Lett.*, 2012, **9**, 02.
39 A. J. Grutter, H. Yang, B. J. Kirby, M. R. Fitzsimmons, J. A. Aguiar, N. D. Browning, C. A. Jenkins, E. Arenholz, V. V. Mehta, U. S. Alaan and Y. Suzuk, *Phys. Rev. Lett.*, 2013, **111**, 087202.
40 R. U. Chandrasena, C. L. Flint, W. Yang, A. R. U. Chandrasena, C. L. Flint, W. Yang, A. Arab, S. Nemšák, M. Gehlmann, V. B. Özdöl, F. Bisti, K. D. Wijesekara, J. Meyerilse, E. Gullikson, E. Arenholz, J. Ciston, C. M. Schneider, V. N. Strocov, Y. Suzuki and A. X. Gray, *Phys. Rev. B*, 2018, **98**, 155103.
41 C. L. Flint, D. Yi, E. Karapetrova, A. T. N. Diaye, P. Shafer, E. Arenholz and Y. Suzuki, *Phys. Rev. Mater.*, 2019, **3**, 064401.
42 C. L. Flint, H. Jang, J. S. Lee, A. T. N. Diaye, P. Shafer, E. Arenholz and Y. Suzuki, *Phys. Rev. Mater.*, 2017, **1**, 024404.
43 G. W. Zhou, Z. Yan, Y. H. Bai, J. L. Zang, Z. Y. Quan, S. F. Qi and X. H. Xu, *ACS Appl. Mater. Interfaces*, 2017, **9**, 45.